Title: Resolving cell lineages and gene functions in the developing mouse gastrointestinal tract using *in utero* transduction

Ziwei Liu[1,‡], Krishnanand Padmanabhan[1,‡], Jingyan He[2,†], Katrin Hector[2], Bettina Semsch[2,3], Jia Sun[3], Viktoria Knoflach[1], Sarantis Giatrellis[2], Khachatur Dallakyan[1], Christian Göritz[2], Emma Rachel Andersson[2,*], Ulrika Marklund[1,*]

[1] Department of Medical Biochemistry and Biophysics, Karolinska Institutet, Sweden

[2] Department of Cell and Molecular Biology, Karolinska Institutet, Sweden

[3] Comparative Medicine, Karolinska Institutet, Sweden

† Current Adress: Janelia Research Campus, Howard Hughes Medical Institute, Ashburn, USA

‡These two authors contributed equally

*These two authors share corresponding authorship

Correspondence:

Ulrika.Marklund@ki.se; Address: Tomtebodavägen 16, 171 77 Stockholm, Sweden. Emma.Andersson@ki.se; Address: Tomtebodavägen 16, 171 77 Stockholm, Sweden.

Keywords: enteric nervous system, gut patterning, neural crest development, lineage tracing, *in utero* transduction

ABSTRACT

How diverse cell lineages emerge and are genetically regulated during organogenesis are central questions in understanding the developmental origins of disease. However, the mouse gut, including its intrinsic enteric nervous system (ENS) derived from migratory neural crest, has remained difficult to experimentally target. Here, we introduce an *in utero* lentiviral nano-injection strategy that enables early and efficient access to progenitor cells of all major cell types within the developing gut as well as gut-innervating ganglia. Leveraging this approach in combination with DNA barcoding and single cell transcriptomics, we resolve clonal relationships in all gut lineages, including epithelial, neural, immune, and mesenchymal cell types. Clonal coupling between distinct subsets of fibroblasts and either pericytes, mesothelial cells, or interstitial cells of Cajal, suggested a developmental logic whereby the mesenchymal compartment arises from a set of fate-biased progenitors. Yet, mesenchymal regionalization along the anterior–posterior axis establishes early, whereas the ENS displays broad clonal dispersion across gut regions and acquires subsequent regional identities. We further adapted the platform for temporally controlled cell-type specific gene manipulation and, as a proof-of-principle, show that induced expression of the proneural factor Ascl1 biases ENS progenitor cells toward neuronal differentiation. Together, this work provides insights into refined spatiotemporal lineage relationships within a multigerm-layer organ and establishes a broadly applicable *in vivo* framework for probing gene function during gastrointestinal and neural crest development.

SIGNIFICANCE

The gastrointestinal tract comprises diverse cell types originating from all three germ layers and includes the neural crest-derived enteric nervous system (ENS). Progress in defining these lineages and their gene regulation is challenged by the limited experimental access to the

51 developing gut. Here, we establish *in utero* lentiviral transduction as an efficient approach to
52 resolve clonal lineages and address gene functions in defined gut cell types. We show that
53 mesenchyme assumes positional allocation early and differentiates through fate-restricted
54 progenitors, linking specialized mesenchymal cell types to different fibroblasts. In contrast, the
55 ENS differentiates stochastically and acquires late regional identities. Our study reveals
56 fundamental principles of multi-lineage organogenesis and provides a framework to dissect the
57 contribution of developmental programs to visceral dysfunction.

58

59 **INTRODUCTION**

60 The gastrointestinal (GI) tract is essential for life. Congenital gut malformations including
61 Hirschsprung disease, pyloric stenosis, and various intestinal atresias result in diverse and life-
62 long complications. In the general population, 30% suffer from chronic gut dysfunctions,
63 including disorders of gut-brain interaction (DGBIs) and inflammatory bowel disease (IBD)
64 (1). Conceivably these conditions may arise from subtle alterations in gut cell composition
65 already established at fetal stages (2). Supporting this notion, premature birth is an identified
66 risk factor for developing DGBIs (3). Furthermore, congenital chronic intestinal pseudo-
67 obstruction (CIPO) can be myopathic, mesenchymopathic or neuropathic (4), underscoring the
68 critical role of coordinated interactions among multiple gut cell types in maintaining GI
69 motility. Thus, there is a need to better resolve how different cell lineages in the GI-tract
70 develop and integrate during early life.

71 Experimental gene perturbation/manipulation - genetic gain or loss of function – are
72 essential tools to resolve how gene regulatory networks control cellular differentiation and how
73 developmental deviations can lead to pathology. Owing to the relative ease with which the
74 central nervous system (CNS) can be genetically manipulated using *in vivo* embryonic
75 transduction or electroporation (5), the CNS field has gained intricate knowledge of precise

76 gene regulatory networks controlling the generation of different neuronal subtypes (6, 7). These
77 manipulations are possible due to the ventricular structure of the brain and the lumen of the
78 spinal cord, making them accessible to plasmids or viral vectors. In contrast, the GI-tract is
79 positioned internally and not possible to target using these common approaches.

80 Normal gut physiology is critically dependent on neuronal control provided by its
81 intrinsic enteric nervous system (ENS), essential for peristalsis, secretion, and blood flow
82 regulation. These functions are modulated by sympathetic innervation, primarily of celiac
83 ganglion neurons, while sensory information is captured from the gut via dorsal root ganglia
84 (DRG) at the trunk regions, and nodose ganglia in cranial regions. The ENS, sympathetic
85 ganglia, and DRG are formed from neural crest cells (NCC), a transient embryonic population
86 originating from the dorsal neural tube (8). In the mouse, delamination of NCC occurs around
87 embryonic day (E)8 (Theiler stages TS12-13) and thereafter, the migrating cells and the ganglia
88 that form are positioned unfavorably for traditional *in utero* manipulations that are typically
89 performed from E11.5 (5). Thus, experimental systems to rapidly investigate the development
90 of the murine gut, the ENS, and other gut-innervating ganglia have been lacking.

91 Recently, we developed neural plate targeting with *in utero* nano-injection (NEPTUNE)
92 to target the developing CNS at earlier stages (9, 10). With NEPTUNE, ultrasound is used to
93 guide lentiviral delivery of cargo into the mouse amniotic cavity as early as E7.5, allowing
94 access to 80-95% of cells in the CNS. The technique can also be used to introduce high-diversity
95 lentiviral barcode libraries to resolve refined lineages using next generation single cell lineage
96 tracing (11, 12). As distinct barcodes integrate in the DNA of each transduced cell, clonal
97 relationships can be reconstructed after successive cell divisions by single cell RNA-sequencing
98 (scRNA-seq), revealing how individual progenitors contribute to the generation of diverse cell
99 types. Here, we asked whether the method allows for targeting of the GI-tract and of neural

100 crest/placodes, whose derivatives innervate the gut, for the purpose of revealing clonally linked
101 gut cell types and performing genetic experimentation of the developing ENS.

102 We found that ultrasound-guided *in utero* lentiviral nano-injection at E7.5 transduces
103 progenitors that contribute to the GI tract, including endodermal (i.e. epithelia), mesodermal
104 (e.g. smooth muscle cells, fibroblasts and interstitial cells of Cajal; ICCs) and ectodermal
105 progenitors (e.g. ENS). In addition, the method efficiently targets extrinsic gut-innervating
106 ganglia (e.g DRG). By combining high-throughput clonal labeling and transcriptomic profiling
107 of cells in the gut, we identified fate-restricted progenitor cells present at the time of
108 transduction and reconstructed lineage relationships across differentiating gut cell types and
109 regions. Of note, we uncovered molecularly defined fibroblast populations that are clonally
110 coupled with either mesothelial cells, pericytes or ICCs, revealing early diversification paths
111 within the gut mesenchyme. We find that ENS targeting is most efficient at early E7.5, but that
112 residual epiblast cells are still present at this stage. Beyond lineage tracing, we show that *in*
113 *utero* nano-injections can be utilized for conditional gene perturbation in the ENS. Using the
114 pan-neuronal Baf53-Cre mouse line, we demonstrate that lentivirus carrying Cre-dependent
115 cargo is selectively expressed in developing enteric neurons. In Sox10-CreERT2 mice,
116 transgene expression can instead be induced in ENS progenitors/glia in a temporally controlled
117 manner. As proof-of-principle, we show that timed overexpression of the proneural
118 transcription factor *Ascl1* promote neuronal differentiation. Taken together, our results show
119 that ultrasound-guided *in utero* nano-injection is a versatile tool to investigate organogenesis
120 and ENS development. Our work offers insight into how neural crest and mesoderm lineages
121 diversify and regionally pattern within the developing gut.

122

123

124

125 **MATERIAL and METHODS**

126

127 **Mice**

128 The following transgenic and reporter mouse strains were used: Baf53b-Cre (JAX, #027826),
129 Sox10-CreERT2 (SER26) (13), R26-EYFP (JAX #006148) and R26-tdTomato (Ai14; JAX
130 #007908). C57/B6J and CD1 (Charles River Laboratories) wild-type (WT) mice were used.
131 Animals were group-housed, with food and water *ad libitum,* under 12-h light-dark cycle
132 conditions, 22°C ambient temperature and 50% humidity. Animal experiments were approved
133 by the local ethics committee (Stockholm Norra djurförsöksetiska nämnd, Jordbruksverket;
134 N5264/18, N6626-2019, N5237-2023, 8188-2017, 2987-2020 and 315-23).

135

136 **Lentivirus constructs**

137 Plasmid *LV-H2B-GFP* was a gift from Elaine Fuchs (Addgene #25999). *LV-EF1A-H2B-*
138 *tdTomato-30N* was previously described (11, 12). *Lenti-DIO-EGFP* (Supplementary Figure
139 1A) was based on the interim vector *pRRLSIN-cPPT-hPGK-EGFP-WPRE* (Gift from Didier
140 Trono, Addgene #12252). *Lenti-DIO-EGFP-Ascl1* (Supplementary Figure 1B) was constructed
141 based on *pRRLSIN-cPPT-shortCAG-dlox-EGFP_2A(PTV)(rev)-dlox-WPRE* and the GeneArt
142 product *mAscl1* (710bp). Both vectors were constructed, amplified, and characterized by the
143 Viral Vector Facility (VVF) of the Neuroscience Center Zurich (ZNZ). Plasmids and virus were
144 produced and characterized as described in (Supplementary Material and Methods). High-titer
145 vesicular stomatitis virus G (VSV-G)–pseudotyped lentiviral particles were produced either in-
146 house or by a commercial facility (GEG TECH, France) and used at a minimum titer of 1×10^9
147 transducing units (TU)/mL.

148

149

150 **Ultrasound-guided *in utero* nano-injections**

151 A detailed description of the procedure has been reported (9, 10) and is described in
152 (Supplementary Material and Methods). We considered Theiler stages TS11A–C to represent
153 the optimal E7.5 window for ultrasound-guided *in utero* injections (Supplementary Figure 4A,
154 B), while injection at E8 or later failed to efficiently target gut and ENS (Supplementary Figure
155 4C, D).

156

157 **Tamoxifen administration**

158 Plug-mated females received tamoxifen (0.1 mg/g body weight; Sigma) dissolved in corn
159 oil/ethanol (9:1) by intraperitoneal injection at E16.0-E16.5. Embryos were collected 26 or 55
160 hours after tamoxifen administration.

161

162 **Tissue preparation and immunohistochemistry**

163 E13.5 embryos were decapitated and fixed in 4% PFA in PBS for 4-5 hours at 4 °C. Intestines
164 from E14.5-E18.5 were dissected out and fixed in 4% PFA in PBS at 4 °C for 1.5-2 hours.
165 Samples were washed in PBS three times and dehydrated in 30% sucrose in PBS at 4 °C
166 overnight. Intestines were cut into 1 cm long pieces, representing different regions and
167 embedded for transverse analysis in OCT freezing medium and stored at -80 °C. Samples were
168 sectioned at 12 µm and stored at -20 °C.

169 Frozen tissue sections were air-dried at RT for 30 min, rinsed with PBS and incubated in
170 blocking solution containing purified donkey anti-mouse Fab (Jackson Laboratories, PA, USA
171 #715-007-003) diluted 1:50 in PBS for 2 hours at room temperature (RT). After rinsing with
172 PBS, the sections were blocked with 2% normal donkey serum (NDS, Jackson) and 0.1% Triton
173 X-100 (Sigma) in PBS for 2 hours, and incubated with primary antibodies diluted in the same
174 solution overnight at 4°C. They were then washed three times with PBS (10 minutes each) and

175 incubated with secondary antibodies at RT for 1 hour. Tissue was washed three times with PBS
176 (10 minutes each) and mounted in DAKO mounting medium (Agilent) containing DAPI (4',6-
177 diamidino-2-phenylindole). Primary and secondary antibodies are specified in (Supplementary
178 Material and Methods.
179

180 **Preparation of single-cell RNA sequencing datasets**

181 CD1 embryos injected with LV-EF1A-H2B-tdTomato-30N were harvested at E16.5. Stomach
182 and 1/3 of the distal small intestine were harvested from the E7.5 experiment, while the
183 stomach, 2/3 of the small intestine, and the entire large intestine were harvested from the
184 E7.5^{Early} experiment. Dissociation was performed as described in (Supplementary Material and
185 Methods). Briefly, tissues were cut, enzymatically processed, triturated and TOM+ DRAQ7-
186 cells isolated through flow cytometry (Supplementary Figure 1C-H). cDNA libraries were
187 prepared using 10x Chromium Next GEM Single Cell 3' Reagent Kits Version 3.1 Dual Index
188 (10x Genomics, CA, USA). The datasets were named according to stage of injection (i) and
189 analysis (a): iE7.5-aE16.5 and iE7.5^{Early}-aE16.5.
190

191 **Analysis of single-cell RNA sequencing datasets**

192 A detailed description of the scRNA-seq analysis can be found in (Supplementary Material and
193 Methods). In brief, E16.5 scRNA-seq datasets were aligned to a combined mouse genome
194 (GRCm38) with a tdTomato-N transgene containing a 30bp barcode region (11, 12) using
195 CellRanger. Raw count matrices were processed in Seurat, with ambient RNA contamination
196 assessed and corrected using SoupX. Low-quality cells and doublets were removed based on
197 gene/UMI thresholds, mitochondrial contents and DoubletFinder predictions. Data were
198 normalized using SCTransform, followed by dimensionality reduction, batch correction with
199 Harmony, clustering and UMAP visualisation. CloneIDs were assigned to cells using the TREX

200 (TRacking and gene EXpression profiling of clonally related cells) pipeline (11, 12) based on
201 shared barcodes. Clonal composition and relationships between cell types were analyzed using
202 statistical comparisons to randomized data, generating clonal coupling scores and correlation-
203 based clustering to infer lineage relationships.
204
205 **Data Accession:**
206 scRNA-seq data used for analysis in Figure 1 and Supplementary Figure 2 can be found at
207 ArrayExpress with the accession number E-MTAB-14817 (11). The scRNA-seq data generated
208 in this study will be made available at GEO upon publication.
209
210
211 **RESULTS**
212 **Efficient targeting of gut-innervating ganglia by *in utero* transduction at E7.5**
213 Previous studies have demonstrated that high-titer lentivirus injection into the amniotic cavity
214 of E7.5 embryos results in widespread transduction of the neural plate and otic placodes (9-11).
215 Because gut-innervating ganglia originate from neural crest or from placodes, we hypothesized
216 that these structures could also be targeted. To assess whether E7.5 amniotic cavity lentiviral
217 injection targets neural plate progenitors that generate gut-innervating neuronal populations
218 (Figure 1A), we re-analyzed a published scRNA-seq dataset of E9.5 and E10.5 embryos
219 injected at E7.5 with lentiviruses carrying *tdTomato* (11). The cells in this dataset had been
220 broadly categorized as "neural tube cells", "epithelial cells", and "neural crest cells" (Figure
221 1B, Supplementary Figure 2A). To investigate whether developing gut-innervating neurons had
222 been targeted (Figure 1D), we renormalized and subclustered the "neural crest cells" (4,916
223 cells), which yielded 14 clusters (Figure 1C, E; Supplementary Figure 2B). We identified three
224 *Tubb3*+ neuronal clusters (clusters 4, 8, 12), while remaining clusters displayed high *Sox10*

225 expression, indicative of neural progenitor or other immature cell states (Figure 1E, F;
226 Supplementary Figure 2C, D). Amongst *Sox10*+ clusters, clusters 0 and 9 were defined as
227 mesenchymal as they expressed *Prrx1* and *Alx1*, while cluster 13 showed a melanocyte identity
228 with high *Mitf* and *Dct* expression. Cluster 6 exhibited an autonomic nervous system character
229 (*Phox2b*+, *Hand2+, Ascl1*+, *Ret*+) containing presumptive sympathetic (*Isl1*+) and ENS (*Isl1-*
230) cells (Figure 1G). The remaining *Sox10*+ clusters lacked unique markers and likely
231 represented progenitor or glial cells; these were annotated as NCC1-NCC7 (Figure 1E).
232 Amongst neuron-enriched clusters, cluster 4 displayed a nodose ganglion identity (*Phox2a+,*
233 *Phox2b+, Tbx1+, Tfap2b-*). Cluster 8 and 12 expressed a DRG profile (*Isl1+, Neurod1+,*
234 *Six1+, Pou4f1+*), with cluster 12 representing an immature state (higher *Sox10* and *Foxd3*
235 expression) (Figure 1E; Supplementary Figure 2C, D).

236 To further substantiate cluster identities, we addressed the Hox gene expression patterns
237 (Supplementary Figure 2E, F). Consistent with a cranial origin, the cluster identified as nodose
238 ganglion exhibited robust anterior Hox gene expression (e.g. *Hoxa1-4*, *Hoxb1-3*). ENS and
239 parts of the sympathetic ganglia originate from vagal neural crest, and cluster 6 expressed a
240 characteristic suite of *Hoxd3-4* and *Hoxb6 (14).* NCC3 lacked Hox gene expression, indicating
241 a rostral cranial identity, while the Hox gene pattern of NCC5 suggested they are
242 progenitors/glia in the nodose ganglion. Posterior Hox gene expression became more
243 pronounced at E10.5, particularly within DRG clusters and several NCC clusters, indicative of
244 the anterior-to-posterior emergence of neural crest derivatives. Together, the data demonstrate
245 that lentiviral injection at E7.5 targets primordia of gut-innervating ganglia, including ENS,
246 sympathetic ganglia, nodose ganglia and DRG (Figure 1D).

247 To confirm that gut-innervating ganglia are persistently labelled, we performed
248 immunohistochemical analysis of E13.5 DRG and E18.5 gut, in embryos injected at E7.5 with
249 lentivirus carrying H2B-GFP. There was robust transduction of the DRG, with efficient

250 labelling of both NeuN+ neurons and SOX2+ progenitors/glia from thoracic to sacral levels
251 (65-83%) (Figure 1H-J). The ENS was uniformly transduced across gut regions, with an
252 average of 51% HuC/D+ neurons and 44% SOX10+ progenitors/glia (Figure 1K-M;
253 Supplementary Figure 3A-D). In addition to ENS labelling, we observed GFP across all gut
254 layers, including in α-SMA+ smooth muscle cells and EpCAM+ epithelial cells (Figure 1N;
255 Supplementary Figure 3E). This indicates that viral particles in amniotic fluid not only
256 transduce the neural plate (ectoderm) but are also in contact with endo- and mesodermal germ
257 cells at E7.5 (Supplementary Figure 4A, B). Indeed, injections during an early developmental
258 window were crucial for ENS targeting, as injections at E8.0-8.5 failed to label both the ENS
259 and gut epithelium, with only sporadic labeling of mesenchymal cells observed (Supplementary
260 Figure 4C, D).

261 Together, these data demonstrate that E7.5 amniotic cavity lentiviral injection enables
262 widespread and stable transduction of the GI-tract, encompassing extrinsic gut-innervating
263 neuronal populations, the ENS, and non-ENS gut cell types.

264

265 ***In utero* transduction targets all major cell types in the developing gut**

266 As we discovered that injections not only target the ENS but the whole gut wall, we reasoned
267 that this approach could be leveraged to determine lineage relationships between gut cell types
268 derived from all three germ layers. Moreover, by capturing different segments of the gut,
269 conclusions could be drawn about the timing of anterior-posterior regionalization. To
270 simultaneously profile the transcriptional identity (cell type) and lineage history (clonality) of
271 single cells, we applied TREX (11, 12) (Figure 2A, B). TREX relies on *in utero* injection of a
272 high-diversity lentiviral library encoding a 30N (random nucleotides) barcode and tdTomato
273 resulting in genomic integration into dividing progenitors, thereby allowing stable inheritance
274 of the construct by all descendant cells. The expression of the barcode under a synthetic

275 ubiquitous promoter allows its detection by scRNA-seq, enabling reconstruction of clonal
276 relationships among captured cells based on shared barcodes (CloneIDs).

277 We injected the tdTomato-30N barcode lentiviral library into the amniotic cavity of
278 E7.5 embryos (Figure 2A) and analyzed at E16.5 (dataset thus called iE7.5-aE16.5). TOM+
279 cells were sorted from stomach and small intestine by flow cytometry and sequenced using the
280 10x Chromium platform (Figure 2B). After removing low-quality cells and potential doublets,
281 5,356 cells were retained for analysis, comprising 3,974 cells from the stomach and 1,382 cells
282 from the small intestine (Figure 2C; Supplementary Figure 5A-C). Cells from both regions were
283 integrated, resulting in eight major clusters defined by canonical lineage markers,
284 corresponding to fibroblast-like cells (*Vim+, Col1a1+, Lum+*), smooth muscle-like cells
285 (*Myh11+, Actg2+, Acta2+*), endothelial cells (*Cd36+, Pecam1+*), foregut basal cells (*Cdh1+,*
286 *Epcam+, Krt5+, Krt15+)*, simple epithelial cells (*Cdh1+, Epcam+, Krt8+, Krt18+*), ENS
287 (*Sox10+, Phox2b+, Ret+, Elavl4+*), immune cells (*Cd52+, Ptprc+*) and mesothelial cells
288 (*Upk3b+, Msln+, Wt1+*) (Figure 2D, E; Supplementary Figure 5D). Further analysis of the
289 simple epithelial cluster revealed predominantly enterocytes (*Vil1+*), along with smaller
290 populations of enterochromaffin cells (*Chga+, Tph1+*), goblet cells (*Clca1+, Fcgbp+*), and
291 intestinal stem cells (*Lgr5+*) (Figure 2F). The 195 ENS cells formed four transcriptionally
292 distinct clusters representing progenitors, neuroblasts, and neurons (Figure 2G). Notably,
293 previously discovered neuronal branches characterized by *Etv1* (Branch A) and *Bnc2* (Branch
294 B) were captured (Figure 2H) (15).

295 Subclustering of the smooth muscle-like cluster revealed a contractile myofibroblast-
296 like state (*Trpc3+, Tagln+*) and a proliferative cluster (Figure 2I, J; Supplementary Figure 5D,
297 E). Subclustering of the fibroblast-like cluster uncovered additional mesenchymal
298 heterogeneity, including Interstitial cells of Cajal (ICC) (*Kit+, Ano1+*), pericytes (*Rgs5+,*
299 *Reln+, Pdgfrb+, Pdgfr*a-) and seven transcriptionally distinct fibroblast subtypes (Figure 21,

300 J). These included proliferative fibroblasts (*Top2a+, Mki67+*), Fibroblast 1 (*Col6a4+,*
301 *Adamdec1+*), Fibroblast 2 (*Fndc1+, Dpt+*), Fibroblast 3 (*Adam12+*), Fibroblast 4 (*Kcnn3+*),
302 Fibroblast 5 (*Mfap5+, Grm3+*) and Fibroblast 6 (*Lepr+, Sp5+*) (Supplementary Figure 5D-H).
303 The proliferative fibroblast cluster likely comprised a mixture of all fibroblast subtypes.
304 Collectively, our results demonstrate that *in utero* lentiviral transduction effectively transduces
305 progenitors of all major gut cell types, encompassing derivatives of the three germ layers
306 (Figure 2K).
307

308 **Barcoded *in utero* transduction reveals clonal lineage structures in the developing gut**

309 The comprehensive capture of diverse gut cell types provided us excellent conditions to reveal
310 detailed lineage relationships. After barcode extraction, 3,959 cells (73.9%) retained CloneIDs
311 (Figure 3A, B; Supplementary Figure 6A-C). Cells with or without CloneIDs showed
312 comparable quality metrics and similar CloneID recovery rates were observed across all cell
313 types, indicating unbiased barcode dropout (Supplementary Figure 6D-G). Most CloneIDs
314 consisted of a single barcode, indicating single lentiviral particle transductions, while up to 4
315 barcodes were detected in a few cells (0.42% of clones) (Supplementary Figure 6H).

316 In total, 1,658 clones were reconstructed and classified into three categories: singletons
317 (1,026 clones), single-cell-type clones (302 clones) and multi-cell-type clones (330 clones)
318 (Figure 3C). Multicellular clones contained on average 4.6 cells and reached a maximum of 31
319 cells (Supplementary Figure 6I). Systematic assessment of multi-cellular clonal compositions
320 per major cell type showed that pericytes, ICCs, smooth muscle and mesothelial cells almost
321 exclusively consisted of multi-cell-type clones (Figure 3C), suggesting substantial lineage
322 diversification. Instead, ENS and immune cells exhibited only single-cell-type clones,
323 reflecting early lineage restriction of their respective precursors. Clone sharing was
324 predominantly found between mesenchymal cell types in the gut, consistent with their shared

325 mesodermal origin (Figure 3D). However, endothelial and mesothelial cells did not share clones
326 with each other despite sharing clones with other mesenchymal cell types, indicating that their
327 progenitor allocation is already distinct at E7.5 (Figure 3D). Cells arising from different germ
328 layers rarely shared clones; only five clones spanned endodermal and mesodermal lineages,
329 likely reflecting residual pluripotent mesendoderm cells (16) at the time of injection (Figure
330 3E).

331 To systematically resolve lineage relationships among refined cell types, we performed
332 clonal coupling analysis by calculating z-scores for deviations in observed clone sharing
333 relative to randomized data. Hierarchical clustering of Pearson correlations between z-scores
334 segregated cell types into broad groups corresponding to germ-layer origin and revealed
335 intricate clonal coupling relations between mesoderm-derived populations (Figure 3F, G,
336 Supplementary Figure 6J, K). Notably, ICCs showed strong clonal coupling with smooth
337 muscle cells and myofibroblasts (Figure 3F-H). This is consistent with previous lineage-tracing
338 studies showing that ICCs and myofibroblasts arise from common precursors and that ICCs are
339 not fibroblasts (17). However, ICCs, myofibroblasts and smooth muscle cells also showed
340 clonal coupling with Fibroblast 4 (*Kcnn3*+). This fibroblast likely corresponds to *Pdfgra*+ cells
341 of the SIP (smooth muscle cells, ICCs, and PDGFRa (18, 19)), recently renamed muscle-
342 embedded interstitial fibroblasts; MIFs (20)) (Supplementary Figure 5E, F). Fibroblast 3
343 (*Adam12*+) showed enriched clonal coupling with mesothelial cells (Figure 3F-H), suggesting
344 an adventitial fibroblast (AF) phenotype (21), further supported by expression of *Wt1* and *Pi16*
345 (Supplementary Figure 5E, G). Fibroblast 1 (*Col6a4+, Adamdec1*+) displayed clonal coupling
346 with pericytes, consistent with the reported localization of *Adamdec1*+ myofibroblasts in the
347 subepithelial space (SEMFs) (Figure 3F-H; Supplementary Figure 5E, H). Notably, clonal
348 coupling analysis thus segregated fibroblast populations into putative contractile, adventitial

349 and perivascular trajectories which was less apparent from transcriptome-based clustering alone
350 (Figure 3H; Supplementary Figure 6L).
351 Clonal coupling patterns among mesoderm-derived populations indicate that
352 mesenchymal lineages diverge early into fate-biased progenitor pools that underpin coordinated
353 tissue patterning during gut morphogenesis (Figure 3H). Collectively, we demonstrate that
354 single-cell lentiviral barcoding at E7.5 recapitulates canonical developmental hierarchies and
355 uncovers early cell fate diversification within the gut, corroborating known lineage
356 relationships while revealing previously unrecognized trajectories contributing to gut
357 organogenesis.
358
359 **Nano-injection at early E7.5 improves ENS targeting while revealing residual epiblasts**
360 Attempting to enrich for ENS targeting, we performed another nano-injection of the N30
361 barcode lentiviral library aimed at an earlier developmental stage ($E7.5^{Early}$, ~TS11b;
362 Supplementary Figure 4A, B), reasoning that primordia of neural crest could be physically more
363 accessible and remain for a longer time before delamination. To gain further information about
364 gut regionalization, we collected stomach, small intestine, and large intestine at E16.5 to
365 generate the $iE7.5^{Early}$-aE16.5 dataset (Figure 4A). Data was processed similarly as in the
366 previous experiment, and we recovered the same major cell types (Figure 4B; Supplementary
367 Figure 7A-E). Notably, the earlier targeting increased the proportion of ENS cells by 7.7-fold
368 (Figure 4C), making ENS the most abundant cell population, and corroborating greater
369 lentiviral accessibility to neural crest primordia at the stage of injection. Higher-resolution
370 clustering further resolved subpopulations within immune and ENS lineages, revealing myeloid
371 (*Lyz2*+, *Mrc1*+, *Cd68*+) and lymphoid (*Trbc1/2*+, *Cd4*+) subpopulations, lymphatic signatures
372 (*Lyve1*+, *Pecam1*+), refined ENS neuron divisions, and Schwann cell precursors (SCPs)
373 (Figure 4D, Supplementary Figure 7F, G).

374 CloneIDs could be assigned to 77.8% of the 21,749 cells (Supplementary Figure 8A-E),
375 yielding 3,421 clones comprising 2,488 singletons, 394 single-cell-type clones, and 539 multi-
376 cell-type clones (Figure 4E). The average and maximum size of multicellular clones were larger
377 in the E7.5^{Early}-aE16.5 dataset (Supplementary Figure 8F). Consistent with the first experiment,
378 mesenchymal populations comprised mainly of multi-cell-type clones, whereas ENS, immune
379 and epithelial populations were more lineage-restricted (Figure 4E). Although most
380 multicellular clones were composed of a single germ layer, a notable fraction (~9%) of clones
381 spanned more than one germ layer derivative (~1.5% spanned all three germ layers; 14 clones)
382 (Figure 4F, G). These cross-germ-layer clones suggest the presence of pluripotent epiblast cells
383 at E7.5^{Early}, in agreement with recent high-throughput spatial transcriptome analyses of murine
384 gastrula (22).

385 The presence of cross-germ-layer clones in the iE7.5^{Early}-aE16.5 dataset complicated
386 lineage relationship analysis between refined cell types, but we reasoned that analysis using
387 germ-layer pure clones would still be relevant. Clonal coupling analysis of pure clones (851
388 clones) recapitulated patterns observed in the iE7.5-aE16.5 dataset (compare Figures 3F with
389 4H; Supplementary Figure 8G). We next restricted analysis to pure mesoderm clones (639
390 clones) (Figure 4I; Supplementary Figure 8H). As previously observed (Figure 3G, H), ICCs,
391 myofibroblasts and Fibroblast 4 (putative MIFs) featured stronger clonal coupling, as did
392 mesothelial cells and Fibroblast 3 (putative AFs) (Figure 4I). Although Fibroblast 1 (putative
393 SEMFs) was not adjacent to pericytes in the correlation heatmap, it exhibited the strongest
394 clonal pericyte coupling of all fibroblasts (Figure 4I; Supplementary Figure 8H). Within the
395 immune population, *Mrc1*+ myeloid and *Trbc1/2*+ lymphoid cells shared only few clones,
396 indicating early lineage specification prior to gut colonization (Figure 4J). The large ENS
397 dataset allowed detailed clonal analysis of ENS subclusters, revealing that many clones
398 consisted of multiple ENS states/types (Figure 4K). Notably, SCPs showed clonal coupling

399 with all ENS subtypes, however less so with the more mature neuron clusters ENC12 and
400 Branch B2 which may differentiate before SCP arrival to the gut (Supplementary Figure 8G).
401 Coupling was overall strong between Branch A and B neurons (Figure 4K; Supplementary
402 Figure 8G, grey box), suggesting no predetermination of either Branch in agreement with an
403 earlier lineage-tracing study (23).

404 Together, our results from the E7.5^{Early} injection highlights the importance of precise
405 embryonic staging for enriched targeting of specific lineage precursors. The optimal window
406 for ENS targeting appears to coincide with early E7.5 (~TS11b stage), when some epiblasts
407 cells are still present. This stage is therefore advantageous for efficient and comprehensive ENS
408 targeting, while posing challenges for lineage analysis.

409

410 **Clonal sharing between gut segments reveals lineage-specific timing of regional identity**
411 **acquisition**

412 Having resolved lineage relationships between and within gut cell types, we next examined the
413 regional dispersion of clones across the upper and lower GI tract. In the iE7.5-aE16.5 dataset,
414 21 clones linking the stomach and small intestine were identified. Of these, 18 clones (85.7%)
415 consisted exclusively of ENS or immune cells, accounting for 25.9% of ENS and 57.9% of
416 immune clones (Figure 5A-C). These regional dispersions are consistent with the extrinsic
417 origins and migratory behavior of these lineages: the ENS arises from neural crest precursor
418 cells that migrate along the entire gut axis (8), while the first wave of embryonic immune cells
419 originates from the yolk sac and subsequently colonizes the gut (24, 25). By contrast, clones
420 corresponding to other cell types were predominantly restricted to a single gut segment,
421 suggesting that most endoderm- and mesoderm-derived progenitors had acquired their regional
422 identities by E7.5 (~TS11c).

423 Considering single-germ-layer clones in the iE7.5^{Early}-aE16.5 dataset, we identified 123
424 region-spanning clones, again mainly from ENS and immune lineages, accounting for 60.7%
425 of ENS and 66.7% of total immune clones (Figure 5D-F). Despite their abundance, epithelial
426 or fibroblast clones did not span regions, indicating that their progenitors are already regionally
427 patterned also at slightly earlier gastrula stages. We next examined the ENS subtype
428 composition within cross-regional and local clones and found them to be similar. Notably, both
429 Branch A and B neurons were present in local and cross-regional clones, supporting the innate
430 stochastic differentiation program in the ENS (Figure 5G). A distinguishing feature of colonic
431 ENS is its expression of *Pou3f3* (26), while it has not been shown if expression is induced in
432 vagally derived enteric *Pou3f3*- precursors as they enter the large intestine. Our barcoding
433 experiment allowed us to clonally link stomach-resident ENS (derived exclusively from the
434 vagal neural crest) to *Pou3f3*$^{+}$ ENS cells in the colon. We found that stomach/large intestine
435 clones distributed randomly amongst ENS differentiation stages and neuron identities (Figure
436 5H). Cells within large intestine-only clones and stomach/large intestine clones showed similar
437 expression frequency and level of *Pou3f3* (Figure 5I). Together, these findings support that
438 colonic ENS cells derived from vagal neural crest acquire their colon-specific identity by
439 responding to local cues.
440
441 **Identification of cell type-specific regional gene expression differences**
442 Beyond lineage relationships, our regionally resolved scRNA-seq datasets enabled analysis of
443 transcriptional similarities and differences across GI regions at E16.5. Integration of the two
444 datasets showed seamless merging (Supplementary Figure 9A, B), indicating consistent
445 targeting of comparable progenitor populations. Most cell types were detected across all regions
446 except for stomach-specific foregut basal epithelia, which expressed distinct marker genes
447 (Supplementary Figure 9C, D). Small intestine epithelium was instead enriched for *Cps1*,

448 whereas posterior Hox genes marked large intestine epithelium (Supplementary Figure 9D).
449 Region-specific expression patterns were also observed in mesoderm-derived populations:
450 *Barx1* and *Nr2f1* were restricted to the stomach, while *Pitx1* was detected in both stomach and
451 large intestine (Supplementary Figure 9E). *Nkx2.3* and *Mab21l2* were confined to intestinal
452 mesenchyme. Within ectoderm-derived tissue (ENS), *Hoxb5*/*Hoxa4* were enriched across
453 intestinal regions, whereas *Hoxc4* was limited to the small intestine (Supplementary Figure 9F).

454 Focused analysis of fibroblast subtypes revealed that Fibroblasts 5 and 6 were enriched
455 in the stomach compared with the intestines (Supplementary Figure 9G, H). Within these
456 populations, *Grm3* and *Sp5* showed stomach-specific expression (Supplementary Figure 9I),
457 whereas Fibroblast 6 uniquely expressed *Thy1* (Cd90), a marker associated with crypt
458 fibroblasts (Supplementary Figure 9I). *Wnt6*, *Cpne8* and *Ism1* in Fibroblast 6 further supported
459 a fibroblast type with high signaling capacity, consistent with a crypt/submucosal-associated
460 niche (Supplementary Figure 9I). These differences may reflect either a greater abundance of
461 Fibroblast 5 and 6 in the stomach or their earlier differentiation in anterior gut regions.

462 In summary, our collective E16.5 scRNA-seq data uncovered regionally distributed cell
463 types, expression patterns and fibroblast states in the embryonic gut, which may contribute to
464 establishing the functional specialization of individual GI regions.

465

466 **Cre-dependent lentivirus nano-injection enables cell type-specific targeting**

467 Our data show that progenitors of essentially all gut cell types are transduced by *in utero*
468 lentiviral nano-injection at E7.5. For applications requiring cell type-specific targeting, this
469 approach therefore needs adaptation. Previous studies have demonstrated that mini-promoters
470 can confer cell type-specificity in the developing CNS (10). However, no ENS-specific
471 promoters have yet been described. Instead, Cre-driver mouse lines have been used to label all
472 or subsets of ENS cell populations.

473 We previously showed that Baf53b-Cre mice specifically label neurons in the juvenile
474 ENS (15). To investigate their utility during embryonic development, Baf53b-Cre; R26-
475 tdTomato embryos were analyzed at two stages (Supplementary Figure 10A, B). Reporter
476 expression was restricted to HuC/D+ neurons and absent from SOX10+ progenitor/glial cells.
477 We found that ~50% of HuC/D+ neurons expressed TOM at E14.5, increasing to ~90% at
478 E18.5. Baf53b-Cre activity is thus confined to differentiating neurons, with a slight delay
479 relative to HuC/D expression.

480 To achieve conditional targeting with *in utero* nano-injection, we designed a lentiviral
481 vector expressing an inverted double-floxed EGFP reporter, Lenti-DIO-EGFP (Figure 6A,
482 Supplementary Figure 1A). While AC injection of non-conditional LV-H2B-GFP resulted in
483 GFP labelling of HuC/D+ neurons, GFP was additionally observed in non-ENS cells as
484 previously discussed (Figure 6B; 1N). In contrast, AC injection of Lenti-DIO-EGFP into
485 Baf53b-Cre embryos resulted in GFP expression restricted to HuC/D+ neurons, labelling ~4-
486 6% at E18.5 (Figure 6B, C). In conclusion, *in utero* nano-injection of conditional lentiviral
487 vectors enables precise targeting of specific gut cell types, as demonstrated by Baf53b-Cre-
488 dependent lentiviral reporter expression in enteric neurons.

489

490 **Timed overexpression of Ascl1 promotes neuronal differentiation of ENS progenitors**

491 Having validated that lentiviral DIO-EGFP expression can be controlled by Cre, we next sought
492 to use this approach to drive timed gene expression in ENS progenitor cells, which are more
493 responsive to developmental cues. Sox10-CreERT2 mice mediate efficient, temporally
494 controlled recombination in ENS progenitors (13, 14, 23). To assess the efficiency and kinetics
495 of Cre-dependent recombination, tamoxifen was administered to Sox10-CreERT2 females
496 mated with R26-EYFP males at E16.5, and embryos were harvested 26 hours later. Out of
497 SOX10+ cells, ~50% expressed EYFP and ~11% of HuC/D+ neurons, indicating efficient

498 labeling of progenitors/glia and a subset of newly differentiated neurons within a short time
499 window (Supplementary Figure 10C-E).

500 As a proof-of-principle, we sought to overexpress *Ascl1*, a proneural transcription factor
501 essential for enteric neurogenesis, as demonstrated by us and others (27, 28). We generated a
502 Cre-inducible *Lenti-DIO-EGFP-Ascl1* construct, in which *Ascl1* was linked to EGFP via a self-
503 cleaving P2A peptide (Figure 6D, Supplementary Figure 1B). Cre-dependent ASCL1
504 expression was validated using a HEK293FT-Cre cell line (Figure 6E). We next overexpressed
505 ASCL1 at late embryonic stages using our system, when both glio- and neurogenesis are
506 ongoing, to assess its ability to promote neuronal differentiation. Sox10-CreERT2 embryos
507 were injected at E7.5 with lentivirus carrying either DIO-EGFP as controls or DIO-EGFP-
508 Ascl1, followed by tamoxifen administration at E16.0 and analysis at E18.5 (Figure 6F). As
509 compared to controls, ASCL1 overexpression reduced the EGFP+ progenitors/glia population
510 (SOX10+ HuC/D-) from ~20% to ~5% (Figure 6G, H) and increased EGFP+ neuronal
511 population (HuC/D+) from ~80% to ~95% (Figure 6G, I). Notably, ~25% of HuC/D+ EGFP+
512 cells in controls co-expressed SOX10, indicative of a transitional population, which was
513 reduced to <5% upon ASCL1 overexpression (Figure 6G, J).

514 Together, these findings demonstrate that ASCL1 overexpression during a gliogenic
515 developmental window is sufficient to bias enteric progenitors toward neuronal differentiation.
516 More broadly, this approach establishes ultrasound-guided *in utero* delivery of Cre-inducible
517 lentiviral constructs as a powerful method for temporally controlled, cell type-specific gene
518 manipulation in developing embryos.

519

520 **DISCUSSION**

521 Our understanding of gut development and related diseases has advanced substantially through
522 recent technologies, including scRNA-seq and spatial transcriptomics (15, 26, 29). However,

523 methods to define lineage relationships and interrogate gene function *in vivo* have lagged
524 behind, partly due to the inaccessibility of embryonic gut using traditional targeting methods.
525 Here, we present ultrasound-guided AC nano-injection as an efficient methodology to access
526 major gut cell populations in mouse embryos, including epithelial and mesenchymal
527 populations, the ENS, as well as gut-extrinsic ganglia. Combined with high-diversity lentiviral
528 barcoding, this approach establishes a versatile lineage-tracing platform, and coupled with Cre-
529 dependent constructs, the approach supports temporally controlled, cell type-specific gene
530 manipulation in the developing gut.

531 Barcode-based lineage tracing combined with scRNA-seq overcomes key limitations of
532 traditional Cre-based lineage tracing approaches as they depend on targeting stem cells defined
533 by single marker genes with often equivocal specificities that risk confounding interpretation.
534 In contrast, the method presented here is unbiased and enables comprehensive reconstruction
535 of lineage relationships. It allowed us to resolve unprecedented details amongst
536 transcriptionally related mesenchymal populations refining their cellular identities, lineage
537 relationships and early development. First, we identified three fibroblast states with distinct
538 clonal relationships to specialized mesenchymal cell types. *Kcnn3*+ fibroblasts – putative
539 contractile fibroblasts (MIFs) – were clonally related to ICCs and myoblast/smooth muscle
540 cells, suggesting shared progenitors. *Adamdec1*+ fibroblasts (putative SEMFs) were linked to
541 pericytes, whereas *Adam12*+ fibroblasts (putative AFs) were clonally related to mesothelial
542 cells. Notably, although previously suggested marker genes were used to annotate fibroblast
543 subtypes, no consensus nomenclature currently exists for gut fibroblasts. Clonal analysis
544 therefore provided important orthogonal support for subtype assignments and supported a
545 developmental logic whereby stromal gut compartments are assembled by a set of fate-biased
546 mesenchymal progenitor populations. Second, by analyzing clonal dispersion across gut
547 regions, we demonstrate that gut mesoderm is already regionally specified along the anterior-

548 posterior axis by E7.5, coinciding with persistent epiblast cells. Third, we present regional
549 diversity amongst mesenchymal cell types, likely reflecting early programs that shape region-
550 specific gut wall composition. Overall, these findings highlight how lineage information
551 complements transcriptomic and anatomical analyses to better define gut stroma development.
552 Increasing evidence shows that different fibroblast subpopulations may have distinct roles in
553 cancer, inflammation, and fibrosis (30), underscoring the importance of better understanding
554 their heterogeneity and development.

555 By integrating multiple gut regions, we found that region-spanning clones were
556 common in migratory lineages such as ENS and immune cells. Within the ENS, clonal sharing
557 across stomach and colon supports a model in which vagal neural crest-derived progenitors
558 acquire region-specific features, such as colonic *Pou3f3* expression, in response to local cues.
559 In contrast, the restriction of epithelial and mesenchymal clones to single regions indicates that
560 regional identity of these compartments is established incredibly early. Together with the
561 region-specific transcriptional programs observed in mesenchymal subtypes, these findings
562 suggest that developmental patterning of the gut wall emerges from a combination of early
563 regional allocation and local differentiation programs.

564 Beyond lineage reconstruction, *in utero* nano-injection enables conditional gene
565 manipulation in defined ENS populations. Using Baf53b-Cre and Sox10-CreERT2 mice, we
566 show that Cre-dependent lentiviral cargo can be activated in differentiating enteric neurons or
567 temporally controlled progenitor/glial populations. Proof-of-principle experiments with *Ascl1*
568 demonstrated that the system can be used to test gene function *in vivo* during defined
569 developmental windows. This approach complements emerging fetal atlases and disease
570 genetics studies, which increasingly identify candidate regulators in transient embryonic cell
571 states but often lack efficient *vivo* validation strategies. We believe that the ability to combine

572 clonal analysis with targeted perturbation can help shift descriptive cell atlas data to mechanistic
573 studies of gut development.

574 Several limitations should also be considered. Our results highlight a strong temporal
575 component of lineage accessibility and commitment. Targeting at E7.5^{Early} enhanced labeling
576 of ENS precursors but also increased cross-germ-layer clones, consistent with presence of
577 epiblast cells. While residual epiblast labeling complicates clonal interpretation, it also provides
578 a functional readout of the developmental window during which germ-layer restriction is being
579 consolidated *in vivo*. Precise embryonic staging is thus essential, and inter-embryo variability
580 can complicate stage estimation, although ultrasound imaging partially mitigates this issue.
581 Tissue dissociation, single-cell capture, and barcode recovery also introduce dropouts that will
582 inevitably reduce clonal reconstruction efficiency. In the gene perturbation setting, conditional
583 targeting efficiencies in the ENS were relatively modest. However, we believe that this
584 mosaicism may in fact be advantageous for studying cell-intrinsic mechanisms given that ENS
585 development depends on coordinated proliferation and long-range migration. Broad
586 perturbation within the ENS may cause large secondary effects at the population level, whereas
587 mosaic manipulation may reveal how genetically altered cells behave within a largely normal
588 developing ENS.

589 Finally, this work has implications for understanding the developmental origins of GI
590 disease. Gut organogenesis relies on interdependent differentiation of diverse cell populations
591 from all three germ layers, and subtle deviations in lineage allocation, maturation, or regional
592 patterning may have lasting functional consequences (31). This is relevant not only to
593 congenital disorders such as Hirschsprung disease, achalasia, and CIPO, but also to more
594 common conditions in which early developmental alterations may predispose to later
595 dysfunction. Some of these disorders may result from *de novo* mutations, in which early
596 mutations occur in a mosaic fashion (32). It is conceivable that the impact of such mutations

597 would be more predictable with a clearer understanding of refined cell lineages arising in post-
598 gastrula stages. We propose that this platform will provide a scalable strategy for mechanistic
599 testing of candidate disease regulators, and modeling early cellular events that may contribute
600 to GI disorders and enteric neuropathologies.
601

602 **ACKNOWLEDGEMENTS**

603 We thank Jonas Frisén and Michael Ratz for designing and sharing the tdTomato 30N barcoded
604 viral plasmids. We also thank Jonas Frisén for access to flow cytometry at Karolinska Institutet.
605 We thank Fernando Lopez-Redondo for laboratory assistance. The authors acknowledge
606 support from the National Genomics Infrastructure in Stockholm funded by Science for Life
607 Laboratory, the Knut and Alice Wallenberg Foundation and the Swedish Research Council.
608 The authors acknowledge the computational resources provided by the National Academic
609 Infrastructure for Supercomputing in Sweden (NAISS), partially funded by the Swedish
610 Research Council through grant agreement no. 2022-06725 and the Centre for Bioinformatics
611 and Biostatistics (CBB) at Karolinska Institutet funded by CIMED Infrastructure and
612 Karolinska Institutet. The imaging was performed at the Biomedicum Imaging Core with
613 support from the Karolinska Institutet. We thank the Viral Vector Facility (VVF) of the
614 Neuroscience Center Zurich (ZNZ) for excellent service, construction and production of Lenti
615 viral plasmids. We thank animal staff from the Department of Comparative Medicine at
616 Karolinska Institutet for help with animals.

617 U.M. was supported by the Swedish Research Council (Vetenskapsrådet; 2020-01129
618 and 2022-01570), the European Research Council (divENSify; 101045026), the Knut and Alice
619 Wallenberg Foundation (KAW; 2020.0109), the Strategic Research Area in Neuroscience, the
620 Strategic Research Area in Stem Cell Research and Regenerative Medicine, Karolinska
621 Institutet (KI) Consolidator Grant, and the Brain Foundation (Hjärnfonden; FO2025-0169;

622 FO2023-0130). E.R.A was supported by KAW (2020.0109), KI Consolidator Grant (2-
623 195/2021), the Strategic Research Area in Neuroscience, Hjärnfonden (FO2025-0271),
624 Vetenskapsrådet 3R grants (2024-03113, 2021-03537, 2017-01054), and the European
625 Research Council (LIMITLESS; 101171156). K.P was supported by Marie Sklodowska Curie
626 Award (1011544005; DeSTENy). K.H, J.H and Z.L were supported by a KI Grant for Salary
627 (2-2110;2019-7;2019-3).

628

629

630 **FIGURE LEGENDS**

631 **Figure 1. Efficient targeting of neural crest/placode populations destined to innervate the**
632 **gut by *in utero* transduction at E7.5.** (A) Schematic drawing of experimental setup for
633 ultrasound-guided *in utero* nano-injection. Left-most panel reproduced from Mangold et al
634 2021 (10), with permission. The right panel was created with BioRender.com. (B) Uniform
635 manifold approximation and projection (UMAP) plot of cells recovered from E9.5 and E10.5
636 embryos following E7.5 amniotic cavity injection (11). (C) UMAP plot of reprocessed neural
637 crest/placode cells (green populations in B), revealing 14 clusters. (D) Schematic drawing of
638 neural crest/placode-derived ganglia innervating the gut. (E) Dot plot showing expression of
639 canonical marker genes for neural crest/placode populations across the clusters. Dot size
640 represents the fraction of cells expressing the gene and color intensity represents mean
641 expression. (F) Feature plots showing expression of neuronal (*Tubb3*+) and migratory neural
642 crest/placode (*Sox10*+) markers. (G) Feature plots showing gene expression associated with
643 nodose ganglia, sympathetic ganglia, DRG and the ENS. (J) Representative
644 immunofluorescence staining of an E13.5 DRG showing H2B-GFP expression in both SOX2+
645 neural progenitors (arrowheads) and NeuN+ postmitotic neurons (asterisks). (I, J) Bar graphs
646 showing proportions of GFP positive NeuN+ neurons and SOX2+ neural progenitors along the

647 thoracic-sacral axis (n=3 mice). Bars represent the mean ± standard deviation (SD). (K)
648 Representative immunofluorescence image of E18.5 small intestine showing GFP expression
649 in HuC/D+ neurons (asterisks) and SOX10+ ENS progenitors and glia (arrowheads). (L, M)
650 Bar graphs showing proportion of GFP positive HuC/D+ neurons and SOX10+ progenitors/glia
651 across gut regions (n=4 mice). Bars represent mean ± SD. Each dot represents one animal. (N)
652 Representative immunofluorescence image of E18.5 gut showing GFP expression in alpha-
653 SMA+ smooth muscle (arrowheads) and EpCAM+ epithelium (asterisks). Scale bars: 50µm.
654
655 **Figure 2. *In utero* transduction at E7. 5 targets diverse cell types in the developing gut.** (A)
656 Schematic of injection of lentiviral barcode library into the E7.5 amniotic cavity. (B)
657 Experimental workflow to generate the iE7.5-aE16.5 dataset consisting of TOM+ cells, flow
658 sorted from two gut regions. (C) UMAP plot of high-quality gut cells colored by tissue of origin.
659 Pie chart indicates the proportion of cells from each region. (D) UMAP plot showing 8 major
660 clusters, annotated based on established marker gene expression. (E) Dot plot displaying
661 expression of canonical marker genes used to define major clusters. (F) Feature plots displaying
662 marker gene expression of epithelial cell types. (G) Reprocessed ENS cells revealing four
663 clusters. (H) Feature plots showing expression of selected markers for ENS states and branches.
664 (I) UMAP plot showing subclusters within fibroblast-like and smooth muscle-like populations.
665 (J) Dot plot showing marker gene expression distinguishing fibroblast-like and smooth muscle-
666 like subclusters. (K) Schematic drawing indicating the diverse gut cell types targeted by *in utero*
667 nano-injection, showing that all three germ layers are efficiently transduced. Part of 2A, B and
668 K were created with BioRender.com. (E, J) Dot size represents the percentage of cells
669 expressing the gene, and color indicates relative mean expression.
670

671 **Figure 3. Lentiviral barcoding at E7.5 resolves clonal lineage relations in the developing**
672 **gut.** (A) UMAP plot highlighting proportions of cells with CloneIDs in the iE7.5-aE16.5
673 dataset. (B) UMAP plot showing 11 major gut cell types after merging subclusters. (C) Stacked
674 bar plot showing distribution of clone categories across major cell types. Schematic drawing
675 describing clonal types (right). (D) UpSet plot showing frequencies of clones with different
676 composition of major cell types. (E) UpSet plot showing minimal clone sharing across germ
677 layers. Inset chord diagrams in (D, E) illustrate the extent and direction of clonal sharing, with
678 ribbon width proportional to the number of shared clones. (F, G) Heatmaps showing the
679 correlation matrix of clonal coupling z-scores, computed as deviations of observed clone
680 sharing relative to randomized data, for refined gut cell types (F) and restricted to mesoderm-
681 derived cell types (G). Colored boxes denote germ-layer origin (pink: endoderm; purple:
682 ectoderm; yellow: mesoderm), or lineage-coupled mesenchymal populations (green: Fibroblast
683 4 with myofibroblasts, ICC and smooth muscle cells; black: Fibroblast 3 with mesothelial cells;
684 brown: Fibroblast 1 with pericytes). (G) Schematic summary of lineage relationships amongst
685 mesenchymal cell types inferred from the clonal coupling analysis. H and left panel of 3C were
686 created with Biorender.com.
687
688 **Figure 4. *In utero* transduction at early E7.5 improves ENS targeting but uncovers**
689 **presence of epiblast cells.** (A) Schematic diagram showing the generation of the iE7.5^{Early}-
690 aE16.5 dataset consisting of three gut regions. Created with BioRender.com. (B) UMAP plot
691 showing major cell types. (C) Alluvial plot showing proportions of major cell types in the iE7.5-
692 aE16.5 and iE7.5^{Early}-aE16.5 datasets. (D) UMAP plot showing refined gut cell type annotations
693 in the iE7.5^{Early}-aE16.5 dataset. (E) Stacked bar plot showing distribution of clone categories
694 across major cell types identified in the iE7.5^{Early}-aE16.5 dataset. (F) UpSet plot showing
695 frequencies of clones with different composition of major cell types. (G) UpSet plot showing

696 notable clone sharing across germ layers. Inset chord diagrams in (F, G) illustrate the extent
697 and direction of clonal sharing, with ribbon width proportional to the number of shared clones.
698 (H, I) Heatmaps showing the correlation matrix of clonal coupling z-scores, computed as
699 deviations of observed clone sharing relative to randomized data, for refined gut cell types (H)
700 and restricted to mesoderm-derived cell types (I). Colored boxes denote germ-layer origin
701 (pink: endoderm; purple: ectoderm; yellow: mesoderm), or lineage-coupled mesenchymal
702 populations (green: Fibroblast 4 with myofibroblasts, ICC and smooth muscle cells; black:
703 Fibroblast 3 with mesothelial cells; brown: Fibroblast 1 with pericytes). (J) Chord diagram
704 showing self- and cross-linking between Mrc1+ myeloid and Trbc1/2+ lymphoid cells. (K)
705 UpSet plot showing co-occurrence of ENS cell states/types in the same clone. Note that Branch
706 B1/2 are not exact equivalents of Branch B1/2 defined in Morarach et al, 2021 (15).
707
708 **Figure 5. Regional clone sharing reveals long-range ENS migration and early regional**
709 **patterning of mesenchymal populations along the GI tract.** (A) UpSet plot showing co-
710 occurrence of major cell types in cross-region clones in the iE7.5-aE16.5 dataset. (B) UMAP
711 plot highlighting cells in cross-region and local clones. (C) Alluvial plot illustrating relationship
712 between tissue region, cell type, and CloneID of the cross-region clones in (A). (D) UpSet plot
713 showing co-occurrence of major cell types in the cross-region clones in the iE7.5^{Early}-aE16.5
714 dataset (restricted to single-germ-layer clones). (E) UMAP plot highlighting cells in cross-
715 region and local clones. (F) Heatmap showing the distribution of clones across gut regions in
716 the iE7.5-aE16.5 dataset, with binary indication of presence or absence. Colored bars denote
717 cell type identities of clones. (G) Heatmap showing clonal composition of ENS cell states/types
718 for cross-region or local clones, revealing no apparent bias. (H) UMAP plot highlighting the
719 differentiation state of clones with different dispersion. (I) Violin plot showing comparable

720 levels of *Pou3f3* expression in colonic ENS cells that are local or share clones with small
721 intestine and/or stomach. Parts of 5A and D were created with Biorender.com.
722
723 **Figure 6. Temporal overexpression of Ascl1 in Sox10+ cells promotes neuronal**
724 **differentiation** (A) Schematic overview of the Lenti-DIO-EGFP vector, before and after Cre-
725 mediated gene inversion. (B) Representative immunohistochemistry images of intestine from
726 wild-type mice injected with LV-H2B-GFP showing GFP expression in both HuC/D- cells
727 (asterisks) and HuC/D+ (arrowheads), and Baf53b-Cre mice injected with Lenti-DIO-EGFP
728 showing GFP expression restricted to HuC/D+ cells (arrowheads). (C) Bar graph showing the
729 percentage of HuC/D+ cells expressing GFP across gut regions in Baf53b-Cre embryos injected
730 with Lenti-DIO-EGFP. (n=5 mice). Bars represent mean ± SD. (D) Schematic drawing of the
731 Lenti-DIO-EGFP-Ascl1 construct with and without Cre-mediated gene inversion. (E)
732 Representative immunohistochemistry images showing validation of transgene expression in
733 Cre-expressing HEK293FT cells. (F) Schematic representation of experimental procedure for
734 *in vivo* overexpression of EGFP-Ascl1 or EGFP in ENS progenitors. Part was created with
735 BioRender.com. (G) Representative confocal images of E18.5 small intestine transduced with
736 DIO-EGFP or DIO-Ascl1-EGFP vectors showing SOX10 and HuC/D expression patterns in
737 GFP+ cells. asterisks denote EGFP+ cells and texts indicate their status of expression, with +
738 or – signs denoting positive or negative expression. (H-J) Bar graphs showing the proportions
739 of GFP+ cells with SOX10 expression without HuC/D (H), GFP+ cells with HuC/D expression
740 (I), and GFP+ HuC/D+ cells expressing SOX10 (J), in Baf53b-Cre embryos injected with either
741 DIO-Ascl1-EGFP or Lenti-DIO-EGFP. (H)*p=0.0136; (I)**p= 0.0086, and (J)* p= 0.011. n=6-
742 7 mice per condition. SI: small intestine; AC: amniotic cavity; WT: wild-type. Scale bars:
743 20µm.
744

745 **REFERENCES:**

746 1. C. H. Knowles, G. Lindberg, E. Panza, R. De Giorgio, New perspectives in the diagnosis
747 and management of enteric neuropathies. *Nat Rev Gastroenterol Hepatol* **10**, 206–218
748 (2013).
749 2. B. Niesler, S. Kuerten, I. E. Demir, K. H. Schafer, Disorders of the enteric nervous
750 system - a holistic view. *Nat Rev Gastroenterol Hepatol* **18**, 393–410 (2021).
751 3. M. P. Sherman, H. Zaghouani, V. Niklas, Gut microbiota, the immune system, and diet
752 influence the neonatal gut-brain axis. *Pediatr Res* **77**, 127–135 (2015).
753 4. S. K. Hashmi, R. H. Ceron, R. O. Heuckeroth, Visceral myopathy: clinical syndromes,
754 genetics, pathophysiology, and fall of the cytoskeleton. *Am J Physiol Gastrointest Liver*
755 *Physiol* **320**, G919–G935 (2021).
756 5. R. Dixit *et al.*, Efficient gene delivery into multiple CNS territories using in utero
757 electroporation. *J Vis Exp* 10.3791/2957 (2011).
758 6. E. Andersson *et al.*, Identification of intrinsic determinants of midbrain dopamine
759 neurons. *Cell* **124**, 393–405 (2006).
760 7. E. Dvoretskova *et al.*, Spatial enhancer activation influences inhibitory neuron identity
761 during mouse embryonic development. *Nat Neurosci* **27**, 862–872 (2024).
762 8. T. Uesaka, H. M. Young, V. Pachnis, H. Enomoto, Development of the intrinsic and
763 extrinsic innervation of the gut. *Dev Biol* **417**, 158–167 (2016).
764 9. K. Mangold, J. He, S. Stokman, E. R. Andersson, Murine Neural Plate Targeting by In
765 Utero Nano-Injection (NEPTUNE) at Embryonic Day 7.5. *J Vis Exp* 10.3791/63148
766 (2022).
767 10. K. Mangold *et al.*, Highly efficient manipulation of nervous system gene expression
768 with NEPTUNE. *Cell Rep Methods* **1** (2021).

769 11. S. de Haan *et al.*, Ectoderm barcoding reveals neural and cochlear
770 compartmentalization. *Science* **388**, 60–68 (2025).
771 12. M. Ratz *et al.*, Clonal relations in the mouse brain revealed by single-cell and spatial
772 transcriptomics. *Nat Neurosci* **25**, 285–294 (2022).
773 13. C. Laranjeira *et al.*, Glial cells in the mouse enteric nervous system can undergo
774 neurogenesis in response to injury. *J Clin Invest* **121**, 3412–3424 (2011).
775 14. F. Memic *et al.*, Transcription and Signaling Regulators in Developing Neuronal
776 Subtypes of Mouse and Human Enteric Nervous System. *Gastroenterology* **154**, 624–
777 636 (2018).
778 15. K. Morarach *et al.*, Diversification of molecularly defined myenteric neuron classes
779 revealed by single-cell RNA sequencing. *Nat Neurosci* **24**, 34–46 (2021).
780 16. V. P. Masamsetti *et al.*, Lineage contribution of the mesendoderm progenitors in the
781 gastrulating mouse embryo. *Dev Cell* **60**, 1991–2006 e1999 (2025).
782 17. S. Torihashi *et al.*, Blockade of kit signaling induces transdifferentiation of interstitial
783 cells of cajal to a smooth muscle phenotype. *Gastroenterology* **117**, 140–148 (1999).
784 18. S. A. Baker *et al.*, Distribution and Ca(2+) signalling of fibroblast-like (PDGFR(+))
785 cells in the murine gastric fundus. *J Physiol* **591**, 6193–6208 (2013).
786 19. S. Schneider *et al.*, Single Nucleus Sequencing of Human Colon Myenteric Plexus-
787 Associated Visceral Smooth Muscle Cells, Platelet Derived Growth Factor Receptor
788 Alpha Cells, and Interstitial Cells of Cajal. *Gastro Hep Adv* **2**, 380–394 (2023).
789 20. S. E. Viitala E.W, Miihkinen M, Chalkidi N, Stavropoulou A, Lemmetyinen TT,
790 Päivinen P, Kaptrio T, Hagström J, Haglund C, Mäkelä TP, Aittokallio T, Katajisto P,
791 Koliaraki V, Ollila S. (2025) High-resolution integrative analysis allows
792 characterization and spatial annotation of normal and cancer-associated colon
793 fibroblasts. (bioRxiv).

794 21. Y. Rinkevich *et al.*, Identification and prospective isolation of a mesothelial precursor
795 lineage giving rise to smooth muscle cells and fibroblasts for mammalian internal
796 organs, and their vasculature. *Nat Cell Biol* **14**, 1251–1260 (2012).
797 22. L. T. G. Harland *et al.*, A spatiotemporal atlas of mouse gastrulation and early
798 organogenesis to explore axial patterning and project in vitro models onto in vivo space.
799 *Cell Rep* **44**, 116047 (2025).
800 23. R. Lasrado *et al.*, Lineage-dependent spatial and functional organization of the
801 mammalian enteric nervous system. *Science* **356**, 722–726 (2017).
802 24. C. C. Bain, A. Schridde, Origin, Differentiation, and Function of Intestinal
803 Macrophages. *Front Immunol* **9**, 2733 (2018).
804 25. W. H. Neo, A. L. M. Lie, M. Z. H. Fadlullah, G. Lacaud, Contributions of Embryonic
805 HSC-Independent Hematopoiesis to Organogenesis and the Adult Hematopoietic
806 System. *Front Cell Dev Biol* **9**, 631699 (2021).
807 26. C. M. Wright *et al.*, scRNA-Seq Reveals New Enteric Nervous System Roles for
808 GDNF, NRTN, and TBX3. *Cell Mol Gastroenterol Hepatol* **11**, 1548–1592 e1541
809 (2021).
810 27. E. Blaugrund *et al.*, Distinct subpopulations of enteric neuronal progenitors defined by
811 time of development, sympathoadrenal lineage markers and Mash-1-dependence.
812 *Development* **122**, 309–320 (1996).
813 28. F. Memic *et al.*, Ascl1 Is Required for the Development of Specific Neuronal Subtypes
814 in the Enteric Nervous System. *J Neurosci* **36**, 4339–4350 (2016).
815 29. M. Zilbauer *et al.*, A Roadmap for the Human Gut Cell Atlas. *Nat Rev Gastroenterol*
816 *Hepatol* **20**, 597–614 (2023).
817 30. N. Chalkidi, C. Paraskeva, V. Koliaraki, Fibroblasts in intestinal homeostasis, damage,
818 and repair. *Front Immunol* **13**, 924866 (2022).

819 31. Z. Zhang *et al.*, Impairment of stromal-epithelial regenerative cross-talk in
820 Hirschsprung disease primes for the progression to enterocolitis. *Sci Transl Med* **17**,
821 eadp4679 (2025).
822 32. M. Mohiuddin, R. F. Kooy, C. E. Pearson, De novo mutations, genetic mosaicism and
823 human disease. *Front Genet* **13**, 983668 (2022).

824

Figure 1

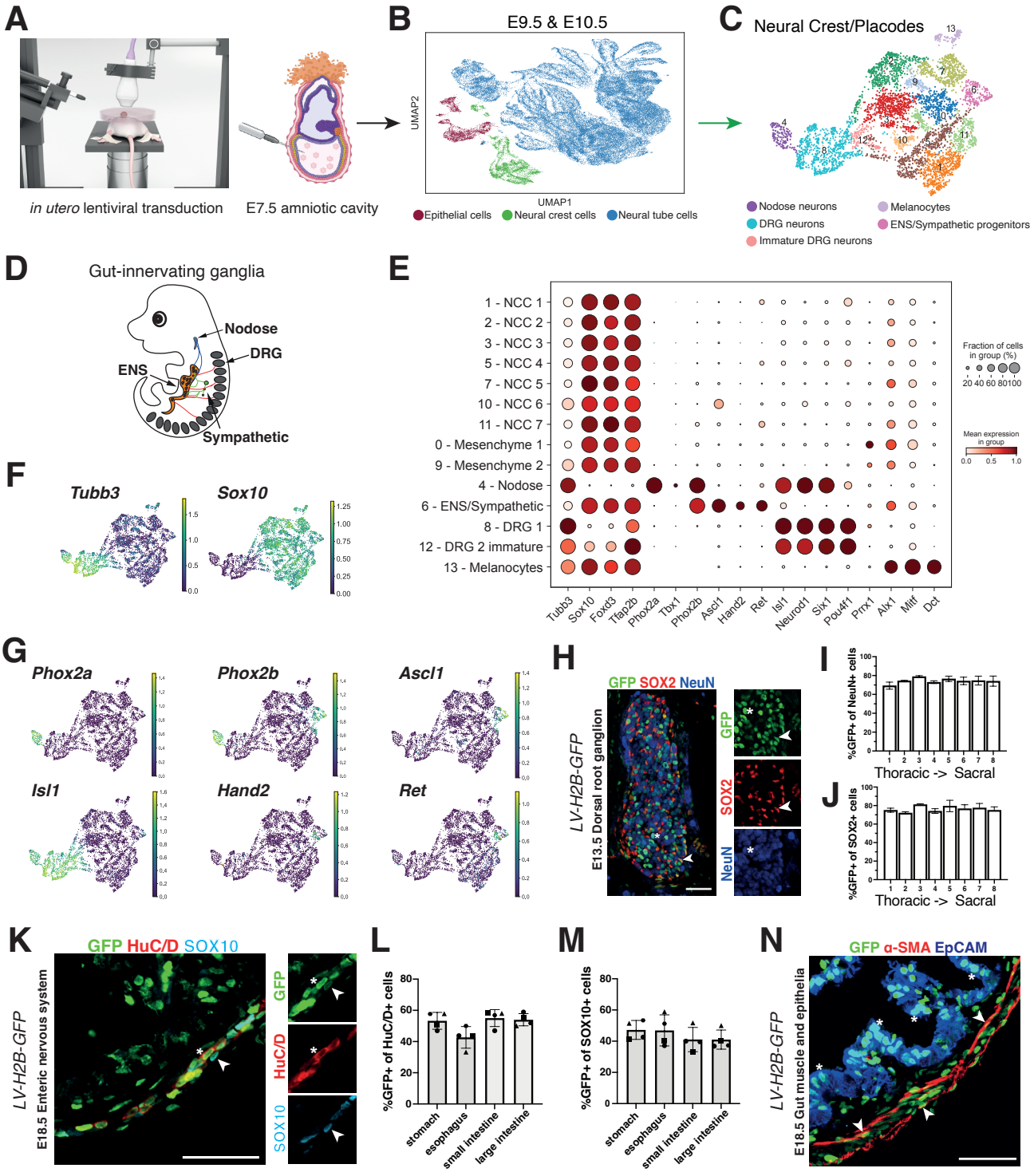
A
in utero lentiviral transduction
E7.5 amniotic cavity
B
E9.5 & E10.5
UMAP2
UMAP1
Epithelial cells
Neural crest cells
Neural tube cells
C
Neural Crest/Placodes
Nodose neurons
DRG neurons
Immature DRG neurons
Melanocytes
ENS/Sympathetic progenitors
D
Gut-innervating ganglia
Nodose
DRG
ENS
Sympathetic
E
1 - NCC 1
2 - NCC 2
3 - NCC 3
5 - NCC 4
7 - NCC 5
10 - NCC 6
11 - NCC 7
0 - Mesenchyme 1
9 - Mesenchyme 2
4 - Nodose
6 - ENS/Sympathetic
8 - DRG 1
12 - DRG 2 immature
13 - Melanocytes
Tubb3
Sox10
Foxd3
Tfap2b
Phox2a
Tbx1
Phox2b
Ascl1
Hand2
Ret
Isl1
Neurod1
Six1
Pou4f1
Prrx1
Alx1
Mitf
Dct
Fraction of cells in group (%)
Mean expression in group
F
Tubb3
Sox10
G
Phox2a
Phox2b
Ascl1
Isl1
Hand2
Ret
H
GFP SOX2 NeuN
LV-H2B-GFP
E13.5 Dorsal root ganglion
GFP
SOX2
NeuN
I
%GFP+ of NeuN+ cells
Thoracic -> Sacral
J
%GFP+ of SOX2+ cells
Thoracic -> Sacral
K
GFP HuC/D SOX10
LV-H2B-GFP
E18.5 Enteric nervous system
GFP
HuC/D
SOX10
L
%GFP+ of HuC/D+ cells
stomach
esophagus
small intestine
large intestine
M
%GFP+ of SOX10+ cells
stomach
esophagus
small intestine
large intestine
N
GFP α-SMA EpCAM
LV-H2B-GFP
E18.5 Gut muscle and epithelia

Figure 2

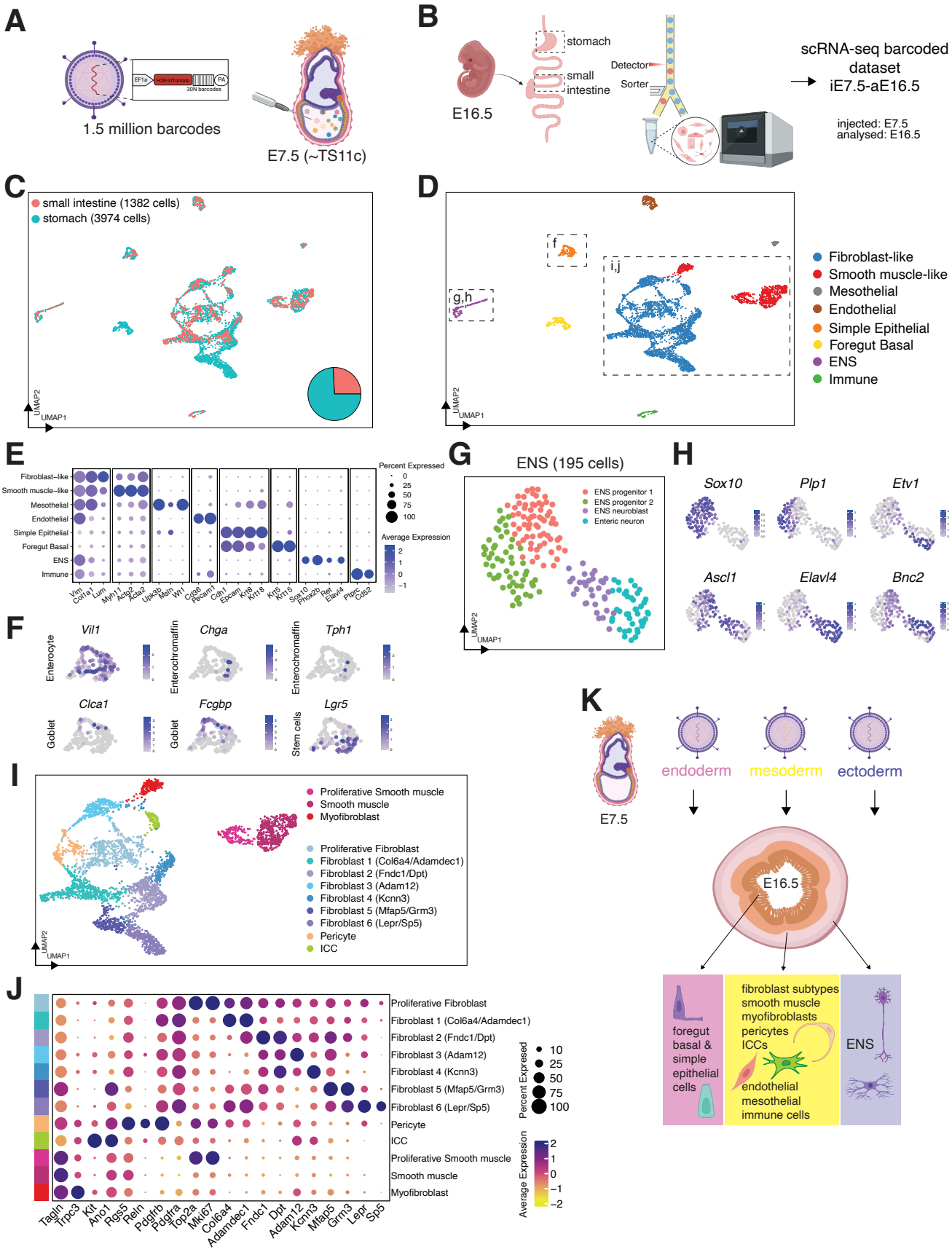
A
1.5 million barcodes
E7.5 (~TS11c)
B
E16.5
stomach
small intestine
Detector
Sorter
scRNA-seq barcoded dataset iE7.5-aE16.5
injected: E7.5
analysed: E16.5
C
small intestine (1382 cells)
stomach (3974 cells)
UMAP2
UMAP1
D
Fibroblast-like
Smooth muscle-like
Mesothelial
Endothelial
Simple Epithelial
Foregut Basal
ENS
Immune
E
Percent Expressed
Average Expression
F
Enterocyte
Enterochromaffin
Goblet
Stem cells
Vil1
Chga
Tph1
Clca1
Fcgbp
Lgr5
G
ENS (195 cells)
ENS progenitor 1
ENS progenitor 2
ENS neuroblast
Enteric neuron
H
Sox10
Plp1
Etv1
Ascl1
Elavl4
Bnc2
I
Proliferative Smooth muscle
Smooth muscle
Myofibroblast
Proliferative Fibroblast
Fibroblast 1 (Col6a4/Adamdec1)
Fibroblast 2 (Fndc1/Dpt)
Fibroblast 3 (Adam12)
Fibroblast 4 (Kcnn3)
Fibroblast 5 (Mfap5/Grm3)
Fibroblast 6 (Lepr/Sp5)
Pericyte
ICC
J
K
E7.5
endoderm
mesoderm
ectoderm
E16.5
foregut basal & simple epithelial cells
fibroblast subtypes
smooth muscle
myofibroblasts
pericytes
ICCs
endothelial
mesothelial
immune cells
ENS

Figure 3

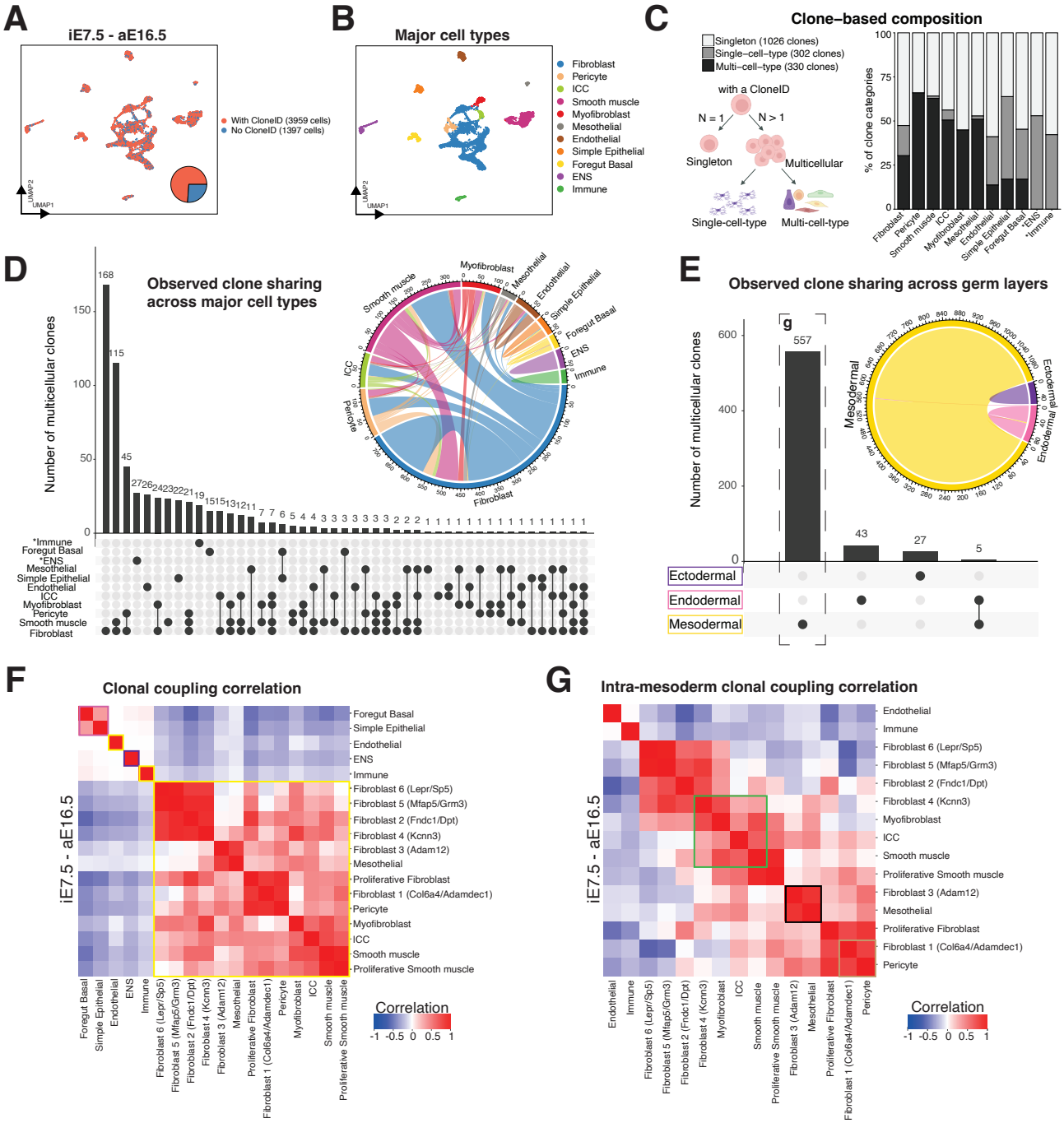
A
iE7.5 - aE16.5
With CloneID (3959 cells)
No CloneID (1397 cells)
B
Major cell types
Fibroblast
Pericyte
ICC
Smooth muscle
Myofibroblast
Mesothelial
Endothelial
Simple Epithelial
Foregut Basal
ENS
Immune
C
Clone–based composition
Singleton (1026 clones)
Single–cell–type (302 clones)
Multi–cell–type (330 clones)
with a CloneID
N = 1
N > 1
Singleton
Multicellular
Single-cell-type
Multi-cell-type
% of clone categories
D
Observed clone sharing across major cell types
Number of multicellular clones
E
Observed clone sharing across germ layers
Ectodermal
Endodermal
Mesodermal
F
Clonal coupling correlation
iE7.5 - aE16.5
Correlation
G
Intra-mesoderm clonal coupling correlation
iE7.5 - aE16.5
Correlation
H
myofibroblast
Muscle-embedded interstitial fibroblast (FB4)
smooth muscle cell
clonal links
Kcnn3
ICC
mesothelial cell
clonal link
Adventitial Fibroblast (FB3)
Adam12
pericyte
clonal link
Subepithelial myofibroblast (FB1)
Col6a4/Adamdec1

Figure 4

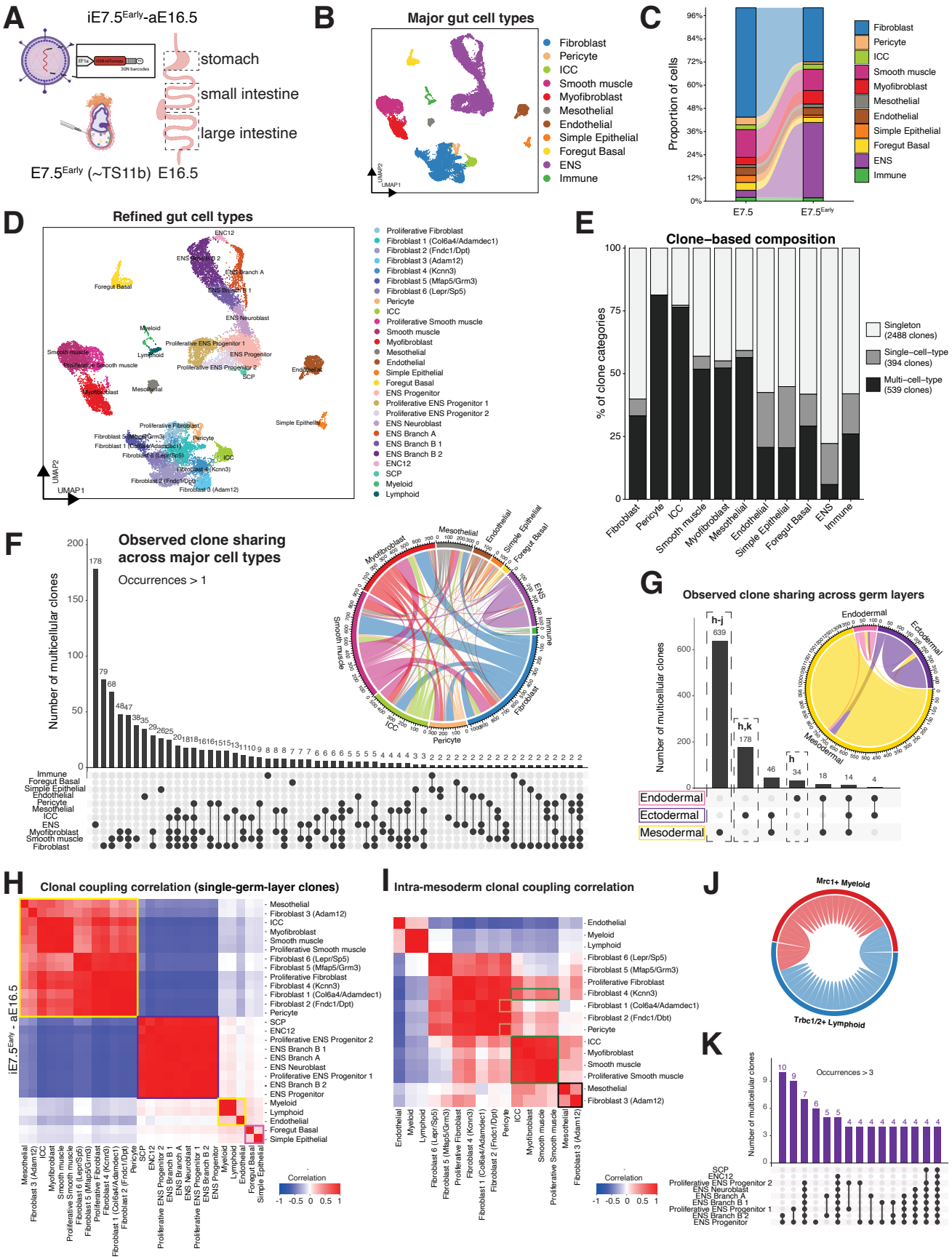
A
iE7.5Early-aE16.5
stomach
small intestine
large intestine
E7.5Early (~TS11b) E16.5
B
Major gut cell types
Fibroblast
Pericyte
ICC
Smooth muscle
Myofibroblast
Mesothelial
Endothelial
Simple Epithelial
Foregut Basal
ENS
Immune
UMAP1
UMAP2
C
Proportion of cells
96%
84%
72%
60%
48%
36%
24%
12%
0%
E7.5
E7.5Early
Fibroblast
Pericyte
ICC
Smooth muscle
Myofibroblast
Mesothelial
Endothelial
Simple Epithelial
Foregut Basal
ENS
Immune
D
Refined gut cell types
ENC12
ENS Branch B 2
ENS Branch A
ENS Branch B 1
Foregut Basal
ENS Neuroblast
Myeloid
Proliferative ENS Progenitor 1
Lymphoid
ENS Progenitor
Smooth muscle
Proliferative Smooth muscle
Proliferative ENS Progenitor 2
SCP
Endothelial
Myofibroblast
Mesothelial
Simple Epithelial
Proliferative Fibroblast
Fibroblast 5 (Mfap5/Grm3)
Pericyte
Fibroblast 1 (Col6a4/Adamdec1)
Fibroblast 6 (Lepr/Sp5)
ICC
Fibroblast 4 (Kcnn3)
Fibroblast 2 (Fndc1/Dpt)
Fibroblast 3 (Adam12)
UMAP1
UMAP2
Proliferative Fibroblast
Fibroblast 1 (Col6a4/Adamdec1)
Fibroblast 2 (Fndc1/Dpt)
Fibroblast 3 (Adam12)
Fibroblast 4 (Kcnn3)
Fibroblast 5 (Mfap5/Grm3)
Fibroblast 6 (Lepr/Sp5)
Pericyte
ICC
Proliferative Smooth muscle
Smooth muscle
Myofibroblast
Mesothelial
Endothelial
Simple Epithelial
Foregut Basal
ENS Progenitor
Proliferative ENS Progenitor 1
Proliferative ENS Progenitor 2
ENS Neuroblast
ENS Branch A
ENS Branch B 1
ENS Branch B 2
ENC12
SCP
Myeloid
Lymphoid
E
Clone–based composition
% of clone categories
100
75
50
25
0
Singleton (2488 clones)
Single–cell–type (394 clones)
Multi–cell–type (539 clones)
Fibroblast
Pericyte
ICC
Smooth muscle
Myofibroblast
Mesothelial
Endothelial
Simple Epithelial
Foregut Basal
ENS
Immune
F
Observed clone sharing across major cell types
Occurrences > 1
Number of multicellular clones
200
150
100
50
0
178
79
68
48
47
38
35
29
26
25
20
18
18
16
16
15
15
13
11
10
9
8
8
7
7
7
6
6
6
6
5
5
5
5
4
4
4
4
4
3
3
2
2
2
2
2
2
2
2
2
2
2
2
2
2
2
2
2
2
2
2
Immune
Foregut Basal
Simple Epithelial
Endothelial
Pericyte
Mesothelial
ICC
ENS
Myofibroblast
Smooth muscle
Fibroblast
Mesothelial
Endothelial
Simple Epithelial
Foregut Basal
ENS
Immune
Fibroblast
Pericyte
ICC
Smooth muscle
Myofibroblast
G
Observed clone sharing across germ layers
Number of multicellular clones
600
400
200
0
h-j
639
h,k
178
46
h
34
18
14
4
Endodermal
Ectodermal
Mesodermal
Endodermal
Ectodermal
Mesodermal
H
Clonal coupling correlation (single-germ-layer clones)
iE7.5Early - aE16.5
Mesothelial
Fibroblast 3 (Adam12)
ICC
Myofibroblast
Smooth muscle
Proliferative Smooth muscle
Fibroblast 6 (Lepr/Sp5)
Fibroblast 5 (Mfap5/Grm3)
Proliferative Fibroblast
Fibroblast 4 (Kcnn3)
Fibroblast 1 (Col6a4/Adamdec1)
Fibroblast 2 (Fndc1/Dpt)
Pericyte
SCP
ENC12
Proliferative ENS Progenitor 2
ENS Branch B 1
ENS Branch A
ENS Neuroblast
Proliferative ENS Progenitor 1
ENS Branch B 2
ENS Progenitor
Myeloid
Lymphoid
Endothelial
Foregut Basal
Simple Epithelial
Correlation
-1 -0.5 0 0.5 1
I
Intra-mesoderm clonal coupling correlation
Endothelial
Myeloid
Lymphoid
Fibroblast 6 (Lepr/Sp5)
Fibroblast 5 (Mfap5/Grm3)
Proliferative Fibroblast
Fibroblast 4 (Kcnn3)
Fibroblast 1 (Col6a4/Adamdec1)
Fibroblast 2 (Fndc1/Dpt)
Pericyte
ICC
Myofibroblast
Smooth muscle
Proliferative Smooth muscle
Mesothelial
Fibroblast 3 (Adam12)
Correlation
-1 -0.5 0 0.5 1
J
Mrc1+ Myeloid
Trbc1/2+ Lymphoid
K
Occurrences > 3
Number of multicellular clones
9
6
3
0
10
9
7
6
5
5
4
4
4
4
4
4
4
4
SCP
ENC12
Proliferative ENS Progenitor 2
ENS Neuroblast
ENS Branch A
ENS Branch B 1
Proliferative ENS Progenitor 1
ENS Branch B 2
ENS Progenitor

Figure 5

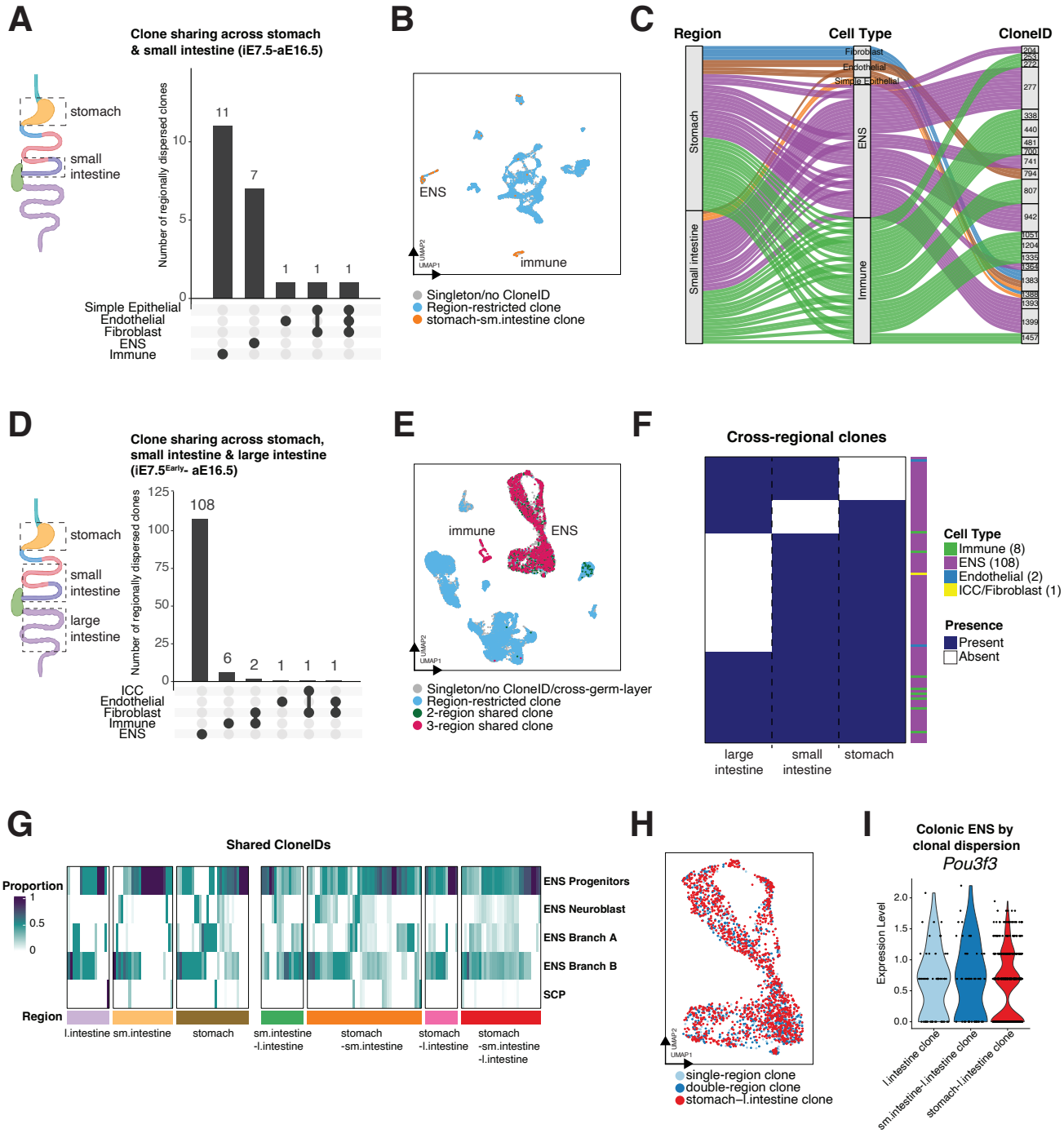
A
Clone sharing across stomach & small intestine (iE7.5-aE16.5)
stomach
small intestine
Number of regionally dispersed clones
11
7
1
1
1
Simple Epithelial
Endothelial
Fibroblast
ENS
Immune
B
ENS
immune
Singleton/no CloneID
Region-restricted clone
stomach-sm.intestine clone
C
Region
Cell Type
CloneID
Stomach
Small intestine
ENS
Immune
D
Clone sharing across stomach, small intestine & large intestine (iE7.5Early- aE16.5)
stomach
small intestine
large intestine
Number of regionally dispersed clones
108
6
2
1
1
1
ICC
Endothelial
Fibroblast
Immune
ENS
E
immune
ENS
Singleton/no CloneID/cross-germ-layer
Region-restricted clone
2-region shared clone
3-region shared clone
F
Cross-regional clones
Cell Type
Immune (8)
ENS (108)
Endothelial (2)
ICC/Fibroblast (1)
Presence
Present
Absent
large intestine
small intestine
stomach
G
Shared CloneIDs
Proportion
Region
ENS Progenitors
ENS Neuroblast
ENS Branch A
ENS Branch B
SCP
l.intestine
sm.intestine
stomach
sm.intestine -l.intestine
stomach -sm.intestine
stomach -l.intestine
stomach -sm.intestine -l.intestine
H
single-region clone
double-region clone
stomach–l.intestine clone
I
Colonic ENS by clonal dispersion
Pou3f3
Expression Level
l.intestine clone
sm.intestine-l.intestine clone
stomach-l.intestine clone

Figure 6

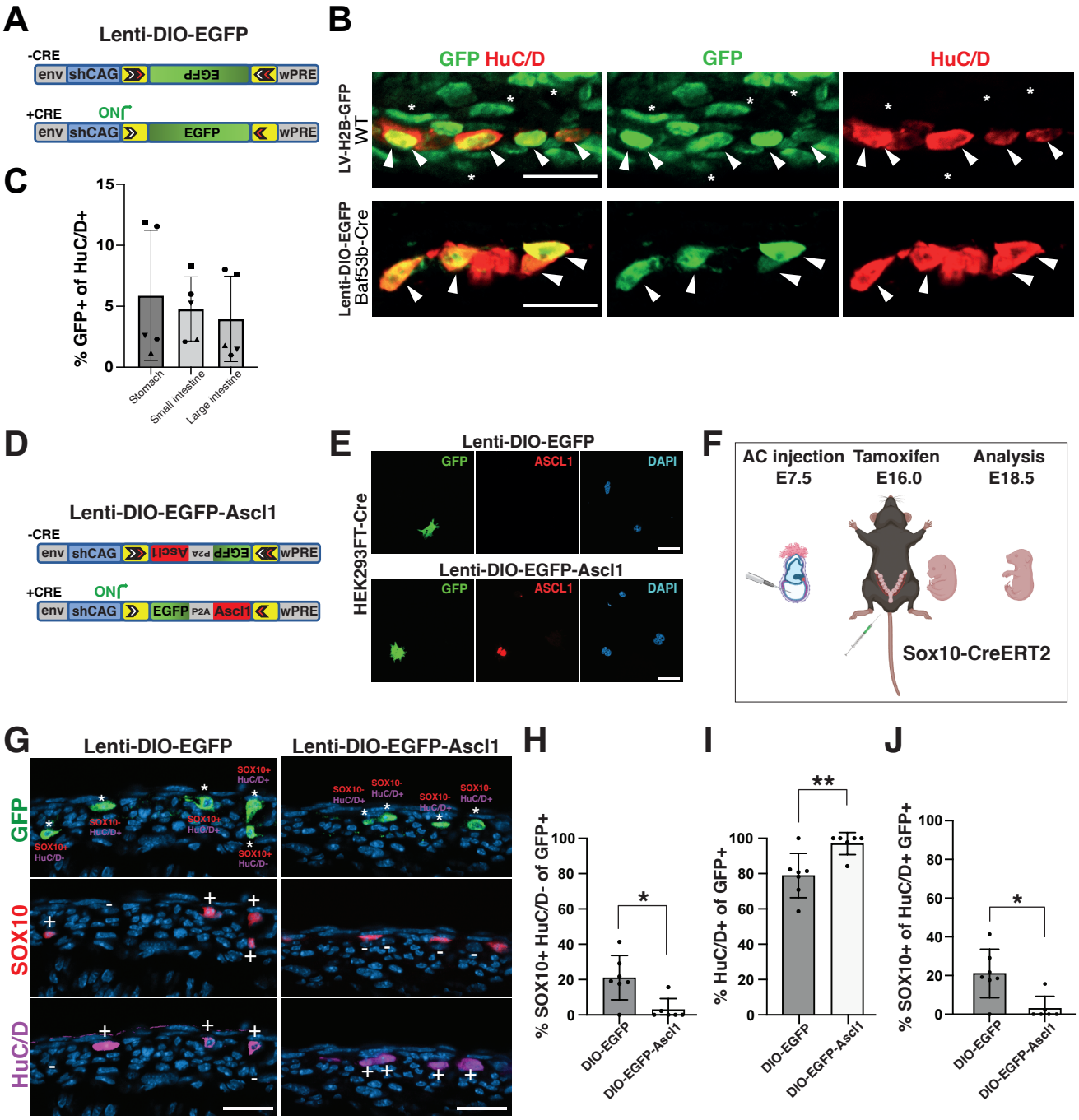
A
Lenti-DIO-EGFP
-CRE
env shCAG EGFP wPRE
+CRE ON
env shCAG EGFP wPRE
B
GFP HuC/D
GFP
HuC/D
LV-H2B-GFP WT
Lenti-DIO-EGFP Baf53b-Cre
C
% GFP+ of HuC/D+
15
10
5
0
Stomach
Small intestine
Large intestine
D
Lenti-DIO-EGFP-Ascl1
-CRE
env shCAG Ascl1 P2A EGFP wPRE
+CRE ON
env shCAG EGFP P2A Ascl1 wPRE
E
Lenti-DIO-EGFP
GFP
ASCL1
DAPI
HEK293FT-Cre
Lenti-DIO-EGFP-Ascl1
GFP
ASCL1
DAPI
F
AC injection E7.5
Tamoxifen E16.0
Analysis E18.5
Sox10-CreERT2
G
Lenti-DIO-EGFP
Lenti-DIO-EGFP-Ascl1
GFP
SOX10
HuC/D
SOX10+ HuC/D+
SOX10- HuC/D+
SOX10+ HuC/D-
SOX10- HuC/D-
H
% SOX10+ HuC/D- of GFP+
100
80
60
40
20
0
*
DIO-EGFP
DIO-EGFP-Ascl1
I
% HuC/D+ of GFP+
**
DIO-EGFP
DIO-EGFP-Ascl1
J
% SOX10+ of HuC/D+ GFP+
*
DIO-EGFP
DIO-EGFP-Ascl1